PROCEEDINGS OF SCIENCE

Search for Lorentz Invariance Violation with time-lag on gamma-ray Cherenkov Telescope data: From the data to the time lag constraints.

Anna Campoy-Ordaz,[b] **Ugo Pensec,**[c] **Cyann Plard,**[d] **Alessandro Armando Vigliano**[e] **and Sami Caroff**[d,*]

[b] *Departament de Física, Universitat Autònoma de Barcelona and CERES-IEEC, Spain*
[c] *Sorbonne Université, CNRS/IN2P3, Laboratoire de Physique Nucléaire et de Hautes Energies, France*
[c] *Laboratoire Univers et Théorie (LUTh), Observatoire de Paris-Meudon, France*
[d] *Laboratoire d'Annecy de physique des particules, Université Savoie Mont-Blanc, CNRS/IN2P3*
[e] *Department of Mathematical, Computer and Physical Sciences, University of Udine, Udine, Italy*
[e] *Istituto Nazionale di Fisica Nucleare (INFN), sezione di Trieste, Trieste, Italy*
E-mail: anna.campoy@uab.cat, ugo.pensec@lpnhe.in2p3.fr, cyann.plard@lapp.in2p3.fr, alessandro.armando.vigliano@ts.infn.it, caroff@lapp.in2p3.fr

Abstract: Slides / Tutorial
Lorentz Invariance Violations (LIV) are allowed within some models of Quantum Gravity and can manifest as energy-dependent effects on photon propagation. This lecture notes aim to provide an overview of LIV data analysis in TeV gamma-ray astronomy, focusing on the estimation of the limits of E^1_{QG} and E^2_{QG} using Cherenkov telescope data. The lecture covers various topics, from the production and propagation of gamma-ray signals, to the detection principles of TeV gamma rays with Imaging Air Cherenkov Telescopes. The importance of data reconstruction and considerations for instrumental effects that can mimic LIV effects are discussed. It particularly focus on the aspect of extraction of time from Cherenkov data, using a likelihood method. Finally, a concrete analysis example using the LIVelihood code is presented, showcasing the extraction of limits on E_{QG}.

Winter School of Theoretical Physics and Third Training School of COST Action CA18108
12–21 February 2023
Pałac Wojanów (Jelenia Góra), Poland,

*Speaker

PoS(QG-MMSchools)009

Contents

1. Introduction

Lorentz Invariance Violations (LIV) are allowed by some models of Quantum Gravity and lead to, in principle observable, energy-dependent effects in the propagation of photons. A particularly interesting case arises from the possibility of having energy-dependent velocities for photons in vacuum. These can be modeled by adding terms to the usual photon dispersion relation as powers of the photon energy over the quantum gravity energy scale. The resulting modified dispersion relation (MDR) to the nth order reads:

$$E^2 = p^2c^2 \left[1 \pm \sum_{n=1}^{\infty} \left(\frac{E}{E_{\mathrm{QG},n}}\right)^n\right], \tag{1}$$

where c is the speed of light in vacuum, p the photon momentum, $E_{\mathrm{QG},n}$ is the typical quantum gravity energy, that is the characteristic quantum gravity energy scale at which LIV phenomena may appear for a given order n. This free parameter is expected to approach the Planck scale energy: $E_P \approx 1.22 \times 10^{19}$ GeV. When a specific order n is chosen, the other higher orders are considered negligible.

If the Hamiltonian equation of motion is still valid, then the particle speed becomes energy-dependent:

$$v_n(E) = c \left[1 \pm \frac{n+1}{2} \left(\frac{E}{E_{\mathrm{QG},n}}\right)^n\right], \tag{2}$$

allowing photons with different energies to propagate with distinct velocities, that is to be super-luminal or subluminal. Then, two photons h and l emitted at the same time by an astrophysical source may arrive on Earth with a delay. This delay at the order n should depend on the energy difference of the photons $\Delta E^n = E_h^n - E_l^n$ and on the cosmology, i.e. the distance traveled. These dependencies are summed up in [1]:

$$\Delta t_n \simeq \pm \frac{n+1}{2} \frac{E_h^n - E_l^n}{H_0 E_{\mathrm{QG},n}^n} \kappa_n^{LIV}(z), \tag{3}$$

where $\kappa_n(z)$ is the propagation term taking into account the universe expansion:

$$\kappa_n^{LIV}(z) = \int_0^z \frac{(1+z')^n}{\sqrt{\Omega_m (1+z')^3 + \Omega_\Lambda}}\, dz',$$

with n the correction order, z the redshift, Ω_m the matter density parameter and Ω_Λ the cosmological constant parameter. Rather than using Equation (3), we can use the time lag per energy, usually written with the units $\mathrm{s} \cdot \mathrm{TeV}^{-n}$, as easier to measure:

$$\tau_n = \frac{\Delta t}{\Delta E_n} = \pm \frac{n+1}{2} \frac{1}{E_{\mathrm{QG},n}^n} \kappa_n^{LIV}(z). \tag{4}$$

The goal of these lectures is to give an overview on gamma-ray astronomy and data analysis, and the process to estimate a limit on $E_{\mathrm{QG},n}$. That is concretely showing how it is performed, starting from the reconstruction of the TeV gamma-ray data obtained by Cherenkov telescopes until getting a limit on $E_{\mathrm{QG},1}$ and $E_{\mathrm{QG},2}$, defining the energy scale at which a Lorentz invariance violation

effect occurs. To do so, the techniques of analysis will be presented as well as the software to extract the result, called LIVelihood.

In the first part, the TeV gamma-ray astronomy will be briefly presented from the source to the observer. This chapter will cover briefly the production, propagation, and detection principle of TeV gamma-ray with the Cherenkov detector technique. In the second part, the data reconstruction will be discussed particularly the usual instrumental caveats to take into account that can mimic the LIV effect. In the end, a concrete analysis will be presented with an example of a limit obtained from simulated data reproducing a H.E.S.S. observed flare of PKS 2155-304.

2. TeV Gamma-ray astronomy

In order to probe the quantum gravity energy, expected to be of the order of the Planck energy, 10^{19} GeV, different astrophysical messengers can be used, among which gamma-ray photons, neutrinos, high-energy protons, or gravitational waves. In particular, gamma rays are good candidates to study the LIV effect thanks to very bright and flaring gamma-ray sources. There are several of them in the universe that we can observe from Earth. This chapter is dedicated to the production mechanisms occurring in these astrophysical sources and how gamma-ray observatories detect them.

2.1 Gamma-ray production mechanisms

This section is mainly based on C. Levy's work [2].

As we can build them on Earth, there are also natural particle accelerators in the universe. Gamma rays are radiated by cosmic-ray particles that non-thermal mechanisms accelerate in these astrophysical sources. The basic scenario for the acceleration of these particles is called the second-order Fermi mechanism and is based on a strong shock acceleration. The resulting spectrum is a power law $\Gamma_S(E) \propto E^{-\alpha}$. These cosmic-ray particles produce highly energetic photons via hadronic and leptonic processes: inverse Compton, synchrotron self-Compton and pion decay are the main contributors to TeV gamma rays. Some other beyond the standard model processes are possible as well but will not be covered by this lecture (*e.g.* dark matter annihilation).

Synchrotron radiation occurs in a medium with a high magnetic field. In its highly magnetized plasma, relativistic charged particles get a radial acceleration from the Lorentz force effect, producing high electromagnetic radiation when the field is strong. The emitted power per unit of frequency P_s depends on the ambient magnetic field strength B and the energy of the particle E as $P_s \propto E^2 B^2$.

The inverse Compton (IC) scattering results from a high-energy electron transferring a part of its energy to a photon when they interact. When the photon energy E_γ is low, such that $E_\gamma < m_e c^2$, the interaction follows the Thomson regime in which the emitted power depends on the electron energy E and the energy density associated with the photon field U_γ as $P_{\rm IC} \propto E^2 U_\gamma$. In a black body approximation, U_γ is temperature dependent. At higher energies, such that $E_\gamma \sim m_e c^2$, the interaction follows the Klein-Nishina regime in which the probability of interaction is lower and the emitted power is $P_{\rm IC} \propto \ln E$. An example of a spectral energy distribution, that is the flux versus the energy, resulting from the IC processus is shown in Figure 1, on which we can see a characteristic peak around 0.1 TeV.

If the inverse Compton processus occurs with photons produced by the synchrotron radiation, this effect is called synchrotron-self-Compton (SSC), and the energy density U_γ is then associated with the synchrotron photon field. In this case, as the synchrotron emitted power P_s is related to the magnetic field strength B, the amount of SSC gamma-rays is directly linked to the magnetic field density $U_B = \frac{B^2}{8\pi}$. An example of a spectral energy distribution from the SSC process is shown in Figure 2. We can see a characteristic peak around 10 eV which results from the synchrotron effect and another one around 100 GeV which results from several phenomena but is dominated by the SSC effect. The relation between synchrotron and IC effects implies a correlation between the synchrotron peak and the IC peak spectra. But if the photon source is external, that is, for example, the IC effect is occurring in a blazar flare but the photon field is external to the flare itself, the two peaks would not be correlated.

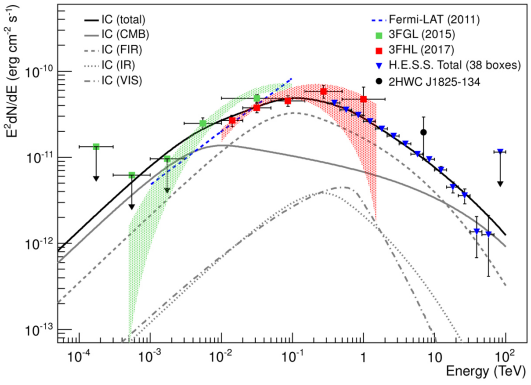

Figure 1: Example of spectral energy distribution resulting from an inverse Compton effect, from nebula HESS J1825–137. It shows the total combined H.E.S.S. energy flux with statistical error bars, the Fermi-LAT spectral fit, and the spectra from the 3FGL and 3FHL catalogues.[3].

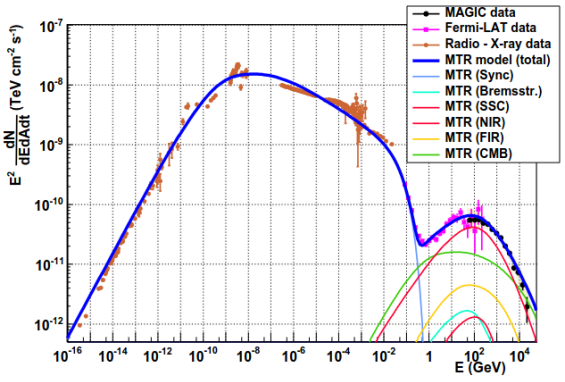

Figure 2: Example of spectral energy distribution resulting from synchrotron and synchrotron self-Compton effects, from the crab nebula. The thin lines show individual components of the photon spectrum, and the thick blue line identifies the overall emission.[4].

Finally, as a common mechanism in all hadronic accelerators, 98% of pion decays result in two photons, which energy depends on the pion velocity: if the pion, produced by hadron-hadron interactions and especially proton-proton interactions, was initially energetic, it may create gamma rays. The spectra of the photons created would be the same as the protons.

2.2 Sources in the LIV search context

To be able to detect LIV effects significantly, we need to maximize the time lag (Equation (4)), that is to use sources with a large range of energy, up to the gamma-ray scale, and at a cosmological distance to maximize z.

With a telescope, we can detect the flux of incoming gamma rays and, to study LIV, we can use a variable flux as a function of time. Indeed, if the variability has a pattern, for example, it can be fitted by a Gaussian, a shift would be visible between low and high-energy photons: a delay between photons with different energies. To do so, three types of sources can be used: gamma-ray bursts (GRB), flaring active galactic nuclei (AGNs), and pulsars.

GRBs are short and transient emissions of photons of all the electromagnetic spectra, including gamma rays. There are short, with a duration shorter to two seconds, and long GRBs, with a duration superior to two seconds [5]. They are extra-galactic, intense, and with a fast variability, so they would be perfect for studying the LIV effect. Unfortunately, they are completely random in space and time, making them very difficult to study.

An AGN is a central supermassive galactic black hole with two-sided relativistic jets of plasma that emit highly energetic photons, that are more visible during flares. When a jet is oriented in our direction, it is called a blazar. They are interesting to study because they are distant sources and the flare can last up to multiple days, but we can not predict when a flare will occur. It is still easier to study than GRBs because we know their position.

Pulsars are highly magnetized rotating neutron stars emitting continuously highly energetic particles along their magnetic axis. This axis is not aligned with their rotation axis and this produces a flashing emission for a distant observer with a period related to the rotation period. The rotation process generates gamma rays with a fast variability. As galactic sources, they have a negligible redshift. Their pulsed emission is difficult to observe at the TeV scale due to the low statistics but can be detected with several hours of observation and has the advantage of being predictable. The fact that their position is known like AGNs enables data to be taken regularly and accumulated over the years.

The LIV effect is a propagation effect and hence independent of the acceleration processes at play in sources. We can then combine all the data we have for sources if the source distance or redshift is known.

2.3 Detection using Cherenkov effect

Gamma rays interact with the atmosphere components, with the result that we cannot see them directly from Earth. One way is to observe them from space, for example with the Fermi-LAT detector. But because the flux is a decreasing power law, we need large surfaces to detect high energies photons, which would greatly increase the cost of an experiment.

The cost of such a sensor makes us come back to Earth, with indirect detection using the atmosphere as a calorimeter. Incoming gamma rays react with the atmosphere components via pair production $\gamma + \gamma \rightarrow e^- + e^+$. The products of this interaction create in turn gamma rays via Bremsstrahlung radiation, which will produce their $e^- - e^+$ pair and so on for a few nanoseconds until a gamma-ray energy drops to about 81 MeV [6]. Gamma rays under this critical energy will be absorbed by the atmosphere via ionization. These series of interactions in the atmosphere are called "cosmic shower", and more specifically electromagnetic shower in case the progenitor particle is a gamma-ray or an electron or positron, and create multiple messengers that we can use: radio, charged particles, fluorescence, or Cherenkov light.

For this course, we are interested in the last one. Cherenkov light is radiation from blue light to UV produced when secondary particles of the shower travel faster than the speed of light in the medium. Water Cherenkov arrays use water tanks to detect the blue light emitted by the secondary particles of the shower when they travel through them. With higher angular and energy resolutions, imaging atmospheric Cherenkov telescopes (IACTs) use the Cherenkov light produced by secondary particles traveling across the atmosphere itself.

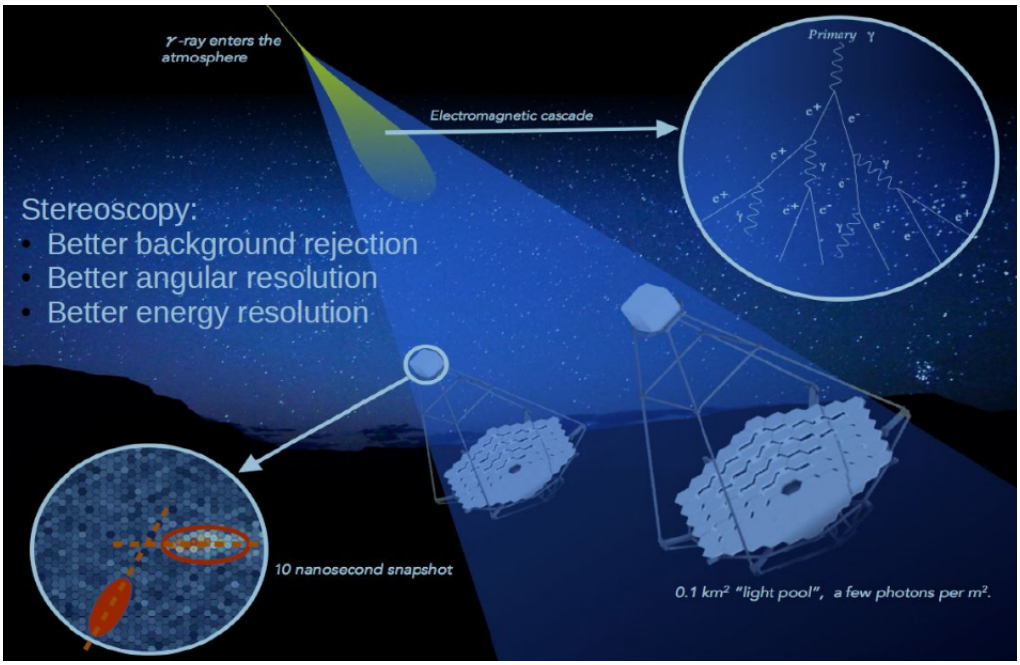

Figure 3: Detection principle using Cherenkov light of the cosmic shower created by an incoming gamma-ray in the atmosphere [7].

The process of its detection is shown in Figure 3. This light forms a cone with a diameter on the ground of approximately 120 meters. The sum of the cones produced by all secondary particles of the shower is visible on the telescope camera as an ellipse. Putting multiple telescopes next to each other as an array may allow them to detect the same shower over different angles, simplifying the reconstruction of the shower's 3D shape. By stereoscopy, it is then possible to reconstruct the arrival direction as well as improve the angular and energy resolutions.

Gamma rays are not the only particles creating cosmic showers in the atmosphere. Hadrons are the most dominant component of cosmic rays (99.9%) and produce showers, called hadronic showers, that can contain a wide variety of particles like pions, kaons, or muons. Their shape is rather chaotic, on the contrary of gamma-ray showers. Indeed, the lateral spread of the electromagnetic showers is largely dominated by Coulomb scattering, while hadronic showers are determined by multiple inelastic scatterings making them less homogeneous.. The secondary particles will get higher transverse momenta so that the lateral spread of hadronic showers is more pronounced. Moreover, hadronic showers produce sub-electromagnetic showers with various intensities, leading to irregular shapes [6, 10]. Figure 4 shows the aspect of these different showers and their corresponding shapes on the camera. These different shapes are used to filter this background.

2.4 Observatories

Current IACTs experiments are H.E.S.S. [11, 12], MAGIC [13, 14], VERITAS [15, 16] and LST-1 [17]. H.E.S.S. is located in Namibia and is composed of four telescopes with a diameter of 12 m and one telescope with a diameter of 28 m. MAGIC is located at La Palma and has

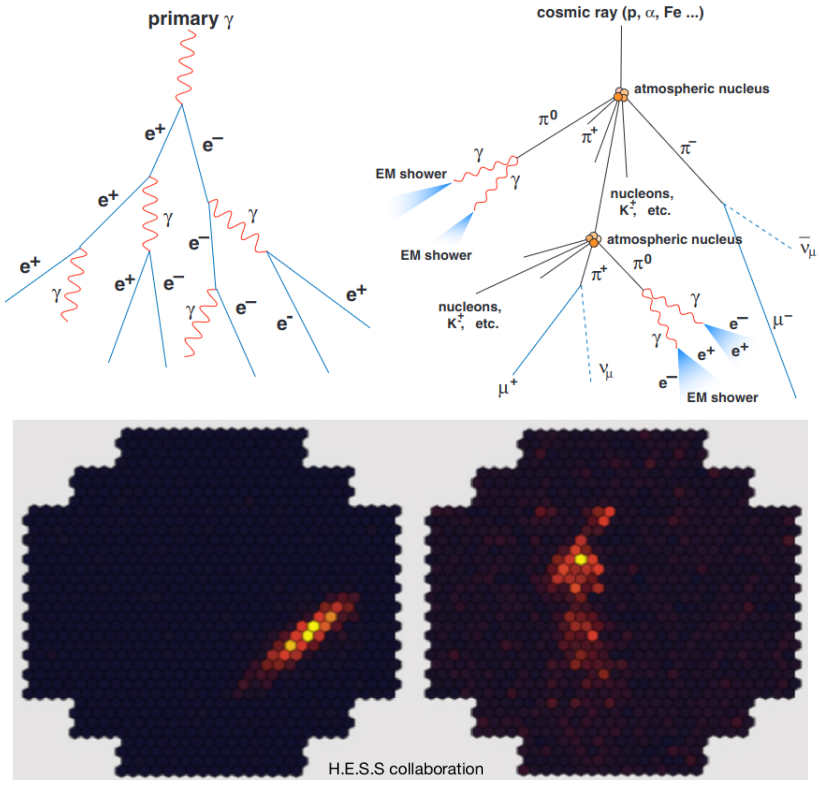

Figure 4: Gamma-ray (left) and hadronic (right) induced shower and their corresponding signal on the camera (bottom) [8, 9].

two telescopes with a diameter of 17 m. Then, VERITAS is in Arizona and is composed of four telescopes of a diameter of 12 m.

CTA [18] is a future array of approximately a hundred telescopes separated in two sites: one at La Palma, in the Canary Islands, and the other in Paranal, in Chile. The end of its construction is expected to be in 2026. It will consist of three types of telescopes: small-sized telescopes (diameter of 4 m), medium-sized telescopes (diameter of 12 m) and large-sized telescopes (LST) (diameter of 23 m). For now, one telescope has been constructed: a LST [19] located at La Palma and currently under commissioning.

3. Data reconstruction

Up to now, we discussed how gamma-ray photons produce electromagnetic showers and how these showers are seen as a Cherenkov light ellipse by IACTs. Then these low-level data go through an analysis pipeline to reconstruct the shower, discriminate between gamma rays and electrons and finally reconstruct the initial photon energy and direction [20]. From this reconstruction, we get a map of the sky in the gamma-ray energy range during the observation. The data is then refined by subtracting the background and selecting the events in the direction of the source. This finally allows to production of the flux variability over time (called hereafter light curve) and the spectrum of the emission. This process will be described here.

3.1 Background subtraction

In order to assess the gamma-ray flux energetic and temporal distribution from a given source, we first need to remove the remaining background events that were not already discriminated by the shower morphology (gamma-like hadrons, electrons and possibly gamma-rays coming from other sources). This background is fortunately isotropic, which helps us determine the background level. We use an observation technique called 'wobble', meaning that the pointing of the telescope is not centered on the region of interest (ROI), but at an offset usually ranging from 0.4° to 1°. Then, during the data analysis, an on region is defined around the tested region, and an off region is defined in a background control region in the field of view (FOV) of the telescope. Different background subtraction techniques can be used based on this procedure (see some of them in [21]).

This off-region must not contain other known sources to avoid contamination. Multiple off-regions can be used. Sampling the number of events in each region, we call them $N_{\text{on}} = N_{\text{s,on}} + N_{\text{b,on}}$

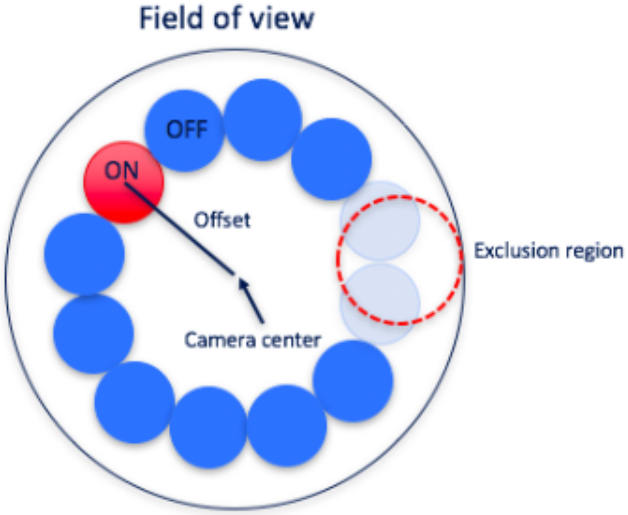

Figure 5: Reflected background technique: the FOV is not centered on the ROI. The on region is defined around the potential source and multiple off regions are defined with the same size around the pointing. An exclusion region is defined because of a nearby source.

and $N_{\text{off}} = N_{\text{b,off}}$, where $N_{\text{s,on}}$ stand for the number of signal events, coming from the studied source if any, in the on region and $N_{\text{b,on}}$ and $N_{\text{b,off}}$ are respectively the number of background events respectively in the on and off region. The isotropy of the background gives $N_{\text{b,on}} = \alpha N_{\text{b,off}}$, where α is the acceptance ratio between ON and OFF regions. Finally, the number of excess events is given by

$$N_{\text{s,on}} = N_{\text{on}} - \alpha N_{\text{off}}. \tag{5}$$

One of these techniques is the reflected background technique (see Figure 5). In this method, the on region of ∼0.1° is defined around the source, and multiple off regions of the same size are reflected around the pointing direction in order to use the radial symmetry of the background (which is due to the radial symmetry of the Cherenkov camera and as well to the radial symmetry of the telescope in general). In the radial symmetry of the background and of the detector response approximations, $\alpha = \frac{1}{\#\text{off regions}}$. It is the most used method to obtain the energy spectrum, mainly because it does

not need to perform an instrumental response function correction between background and signal region which allows to minimize systematical uncertainties. However, it is difficult to use it with a large ROI, given the geometrical pattern of the OFF regions, particularly if multiple exclusion regions need to be defined in the field of view.

3.1.1 Statistics and significance

Given the fact that, in search of LIV, the preferred sources are gamma-ray sources placed at the farthest distances with the highest energetic photons in order to maximize the magnitude of the expected photon delay and therefore the chances to detect it, statistics are limited. Accordingly, the selection of the analysis method is crucial to make optimal use of the available data [22].

The Maximum Likelihood Estimation (MLE) is a hypothesis-testing technique that can be applied to any observed data set to estimate a set of parameters of interest describing an assumed probability distribution. Maximizing the likelihood function under the presumed statistical model, the set of parameters obtained is such that the observed data are the most probable.

However, like any other statistical test, maximum-likelihood estimators require deep comprehension of the probability distribution of the hypothesis, which is generally a limiting fact in research. But Wilk's theorem states a convenient and consistent result.

For a model with N parameters and the sample size approaching ∞, under the null hypothesis H_0, the distribution of the test statistic will asymptotically follow a chi-squared (χ^2) distribution with r degrees of freedom equal to the dimensional difference between the assumed parameter space Θ and the one associated to the null hypothesis Θ_0:

$$\mathrm{TS} = -2\ln\lambda \sim \chi^2(r); \tag{6}$$

being λ the likelihood ratio is defined as follows:

$$\lambda = \frac{\text{likelihood for null model}}{\text{likelihood for testing model}} = \frac{\mathcal{L}(X|\Theta_0)}{\mathcal{L}(X|\Theta)}\ . \tag{7}$$

As an approximate statistical test, the χ^2 value corresponds to the desired statistical significance. This means that even though we can not definitively determine if the null hypothesis is true, we can dismiss it with a certain level of sensitivity ($\sqrt{TS}$).

Regarding the current issue, where the observed values refer to the observed data $X = (N_{\mathrm{on}}, N_{\mathrm{off}})$, the expectation of the number of source photons and the expectation of the number of background photons are unknown parameters $\Theta = (\langle N_{\mathrm{s,on}}\rangle, \langle N_{\mathrm{b,off}}\rangle)$. In this scenario, the null hypothesis H_0 would be the fact that all the observed photons were background photons, meaning no actual gamma-ray source exists and so $\langle N_{\mathrm{s,on}}\rangle = 0$. Further details and explicit extended calculations can be found at [23].

3.2 Instrumental response functions

Now we need to take into account how the instrument can distort the source. The Instrumental Response Functions (IRFs) are a set of functions describing the behavior of the telescope and the reconstruction software to an event. It contains the effective area and the energy migration. It acts as an effective model computed for a given telescope setting by experimentalists from Monte-Carlo

simulations of the whole interacting processes: atmospheric shower, production of Cherenkov light, the reflection of the mirror and camera electronics response. Many things are in fact hidden behind these (see Julien Bolmont's lecture [20]): calibration for each pixel, correcting mirror alignment, variability of atmospheric showers, electronic dead time, trigger threshold (minimum 3 pixels activated), atmospheric transparency, telescope structure bending, night sky background light, among other things, which is why they are very useful.

The effective area is the area of collection of the instrument corrected from the probabilistic loss of events due to the instrument and data reconstruction (this probability of event loss versus energy is called efficiency). . This correction depends on the energy of the photon and can change over time. Indeed, the zenith angle of the source will vary during observation. Since observation conditions and instrumental performance changes with the zenith angle, the zenith angle variability is an important source of instrumentally induced variability. This effect can mimic a time lag in the data, so they need to be taken into account.

The energy migration describes how the energy is reconstructed by the instrument as a function of the true energy of the gamma-ray photon. There is an uncertainty in the reconstruction (due to electronic noise for example), and there could be a bias (because of attenuation of the reconstructed energy from missing light for instance).

Taking into account these IRFs allow us to correct the instrumental effect affecting the measurement, get as close as possible to the true value of the measured quantity.

3.3 Data analysis

Now that the background is removed and the instrumental effect on the observed number of gamma-rays is corrected, we can compute the light curve and the spectra of the source.

The light curve is the flux of the source as a function of time $\phi(t)$. It can be expressed using the effective area A_{eff}, the time migration matrix M_t encoding how the arrival time of the photon is reconstructed and the probability density function (PDF) of distribution of photons versus time detected by the telescope $\frac{\mathrm{d}P}{\mathrm{d}t}(t)$, as

$$\frac{\mathrm{d}P}{\mathrm{d}t}(t) = \frac{1}{N}\int_{-\infty}^{+\infty} A_{\text{eff}}(t')M_t(t,t')\phi(t')\mathrm{d}t', \tag{8}$$

where N is the normalisation constant of the PDF. Considering that the time migration matrix M can be simplified as a Dirac δ distribution (time resolution is $\sim$ 10ns,) Equation (8) can be expressed as :

$$\frac{\mathrm{d}P}{\mathrm{d}t}(t) = \frac{1}{N}A_{\text{eff}}(t)\phi(t). \tag{9}$$

The idea is the same for the spectrum of the source Γ_S. The spectrum is expressed from the effective area A_{eff}, the energy migration matrix Mig, and the probability density function of photons as detected by the telescope $\frac{\mathrm{d}P}{\mathrm{d}E}(E)$, as :

$$\frac{\mathrm{d}P}{\mathrm{d}E}(E) = \frac{1}{N}\int_{0}^{+\infty} A_{\text{eff}}(E')\text{Mig}(E,E')\Gamma_S(E')\mathrm{d}E'. \tag{10}$$

The spectrum is often assumed to be a power law $\frac{\mathrm{d}P}{\mathrm{d}E}(E) \propto E^{-\alpha}$.

So finally, with time and energy variability,

$$\frac{\mathrm{d}^2P}{\mathrm{d}E\mathrm{d}t}(E,t) = \frac{1}{N}\int_0^{+\infty} A_{\mathrm{eff}}(E',t)\mathrm{Mig}(E,E')F(E',t)\mathrm{d}E'. \tag{11}$$

We generally assume no significant time-dependent spectral variability in a short time scale, such that

$$F(E,t) = \Gamma_S(E)\phi(t). \tag{12}$$

But this general description could not work with time-dependent spectra, which we expect to see with the next generation of IACTs . In this case, we can replace $\Gamma_S(E)$ by $\Gamma_S(E,t)$ in the previous equation or even work with a fully time and energy-dependent model $F(E',t)$.

4. LIV analysis

The performance of time-lag measurements depends primarily on five factors. An excellent time resolution is fundamental for the measurement of the time delay between the arrival of photons of different energies, directly impacting the performance of the analysis. For modern IACTs time resolution can arrive at the order of the nanosecond, being limited only by the poor statistics of the photons for the observed events. A good angular resolution has, at most, a marginal impact on LIV analysis to the extent that a better resolution reduces the background and improves the detectability of point-like sources. The Gamma/Hadron separation is extremely important to lessen the background of the measurement, improving again the detectability of the sources.

Finally, point-like, transient sources must be properly aimed in order to catch their signal. This is governed by two factors: the FOV size and the slewing speed of the telescope. A bigger FOV size permits to catch more easily transient events, making it easier to follow up on external alerts and reducing the number of pointings required to cover the localization error region provided with the alerts. A high slewing speed is then fundamental to catching the earliest phases of the emission (the prompt emission) of transient events. Since during the prompt phase the highest energies are emitted in a very short time this is the ideal scenario for time of flight studies and the ability to observe this phase of the emission allows to put really strong constraints on potential LIV effects. Table 1 shows the FOV values and slewing speeds for the current and future generation of IACTs.

	Veritas [24]	MAGIC [25]	H.E.S.S. [26]	LSTs [27]	MSTs [28]	SSTs [29]
FOV size	3.5°	3.5°	5°	4.3°	7.6°	10.5°
Slewing speed	1°/s	7°/s	1.7°/s	12°/s	4°/s	6°/s

Table 1: IACTs FOVs and slewing speeds.

Because of the small FOVs of IACTs, time-of-flight studies are extremely dependent on external alerts to observe sudden transient events. This is very limiting because the observations depend on the promptness of the alerts convoluted with the slewing speed of the telescope, the dimensions of the localization error region of the alert that needs to be covered in order to identify the source, and a good dose of luck. Obviously the lower the observation delay, the better will be the variability and the statistics. On the contrary, high energy and flux sensitivities are fundamental for LIV data analysis. As low energy gamma rays are the most important in order to catch transient events, due to

the absorption of extragalactic gamma rays due to the interaction with the Extragalactic Background Light (EBL) [30], the lower the observable flux ($\mathrm{erg{\cdot}cm^{-2}{\cdot}s^{-1}}$) the more transient sources can be observed. A good energy resolution directly impacts the measurement as it allows to correctly characterize the energies of incoming photons and it acts on the LIV analysis in the same way as adding stochasticity in the time lag. This means that a better energy resolution increases the detectability of the lag, and this effect is even stronger for LIV orders above the first.

4.1 Intrinsic time delay

When we are searching for a delay between the arrival of two photons of different energies, we assume that they were emitted at the same time by the source. But in fact, we have no guarantee for this, and several astrophysical effects can mimic a LIV effect, such as echoes during the pair production or different acceleration time scales between high and low energies particles. Then, the total time lag is expressed by :

$$\Delta t = \Delta t_{\mathrm{LIV}} + \Delta t_{\mathrm{IGMF}} + \Delta t_{\mathrm{source}}, \tag{13}$$

with Δt_{LIV} the time lag induced by Lorentz Invariance Violation effect, Δt_{IGMF} the time lag induced by the intergalactic magnetic field electron pair production and $\Delta t_{\mathrm{source}}$ the delay at the source due to the acceleration/cooling mechanisms at play. So far, since we did not find any significant time delay in the data, we can consider that these lags induced by those effects are compatible with zero given the current precision of the current experiments. Moreover, the intergalactic magnetic field (IGMF) implies a difference of source morphologies, due to the diffusion of the charged electron/positron pairs [31], which is not expected for the LIV, allowing a distinction between the two effects. Anyway, a stochastic argument would be that source intrinsic effects should be different between all types of sources and flares so by combining the data of all sources we have, it can be counterbalanced. Also, the more the redshift increases, the more it is possible to distinguish the different effects due to the increasing LIV effect, which means that analysis on multiple sources at multiple redshifts can be of great help to tackle this challenge.

4.2 The likelihood method: LIVelihood

As mentioned in previous sections, LIV searches benefit from large samples with diversification of source types and distance scales. For that purpose, to provide a standardized analysis method for LIV time-of-flight studies, the production of a common and not yet public software in ROOT C++ named after *LIVelihood* was done.

For the first time, the analysis will be performed with the combination of all relevant data from three leading Imaging Atmospheric Cherenkov Array (H.E.S.S., MAGIC & VERITAS) and the new era of CTAO experiment (more concretely LST-1); joining the analysis of AGNs, pulsars and GRBs. In that sense, an MoU has been signed between the mentioned experiments to share data for LIV searches and this section will be mostly based on the first paper of such collaboration [32].

For a new experiment with such implications, the methodology and the ingredients needed must be taken into account accurately and therefore explained in detail.

Going back to Equation (3) and the parameter of interest τ_n (Equation (4)) that quantifies the LIV effects for a source placed at a specific distance $\kappa_n(z)$, we need to redefine the time lag

parameter for being "distance-independent" in order to perform combinations between multiple sources. Thus, the introduction of a new parameter which is redshift independent noted λ_n is crucial:

$$\lambda_n = \frac{\tau_n}{\kappa_n(z)} = \frac{\Delta t}{\Delta E_n \kappa_n(z)} = \pm \frac{n+1}{2H_0 E_{QG}^n}, \tag{14}$$

with $\Delta E_n \equiv |E_i^n - E_j^n|$, and λ_n being expressed in the same units as τ_n (s/TeV^n).

The correction in redshift allows computing distance lag analyses for different model assumptions. LiVelihood software is designed to test the two following approaches but any other model can be easily implemented.

$$\kappa_n^{J\&P}(z) \equiv \int_0^z \frac{(1+z')^n}{\sqrt{\Omega_m (1+z')^3 + \Omega_\Lambda}} dz' \tag{15}$$

$$\kappa_n^{DSR}(z) \equiv \int_0^z \frac{h^{2n}(z')\, dz'}{(1+z')^n \sqrt{\Omega_m (1+z')^3 + \Omega_\Lambda}}, \tag{16}$$

with

$$h(z') \equiv 1 + z' - \sqrt{\Omega_m (1+z')^3 + \Omega_\Lambda} \times \int_0^{z'} \frac{dz''}{\sqrt{\Omega_m (1+z'')^3 + \Omega_\Lambda}}. \tag{17}$$

The two distributions $\kappa_n^{J\&P}$ and κ_n^{DSR} for the linear n=1 and quadratic n=2 correction orders are depicted in Figure 6 as a function of redshift z. For small z, the two models are consistent and the ratio $\kappa_n^{J\&P}/\kappa_n^{DSR}$ approaches unity as z tends towards zero. However, the distinction between the two models becomes more and more obvious as z increases.

In order to extract limits on $E_{QG,n}$ and search for linear and quadratic LIV delays, the ML method described in Section 3.1.1 is employed. It is based on building a probability density function (PDF) that estimates the probability of observing a gamma-ray photon with a specific arrival time and reconstructed energy. The profile likelihood reads as follows:

$$L(\lambda_n) = \sup_{\vec{\theta}} L\left(\lambda_n, \vec{\theta}\right) = \prod_i \frac{dP\left(E_{i,m}, t_i; \lambda_n\right)}{dE_{i,m} dt_i}. \tag{18}$$

The PDF's simplest expression (Equation (19)) for signal photons is represented in terms of time and energy with the distance time delay λ_n being the only parameter to estimate and with the instruments taken as perfect, supposing that the measured energy is taken as the true photon energy ($E_t \equiv E_m$) and no migration matrix or effective area is required :

$$P_s(E_t, t; \lambda_n) = \frac{\Gamma_s(E_t)\, C_s(t - D(E_t, \lambda_n, z))}{N_s}. \tag{19}$$

The first term refers to the energy spectra of the source, followed by the LIV-transformed light curve where E_t is the true energy of the gamma-ray photon and t is the arrival time corrected by the factor

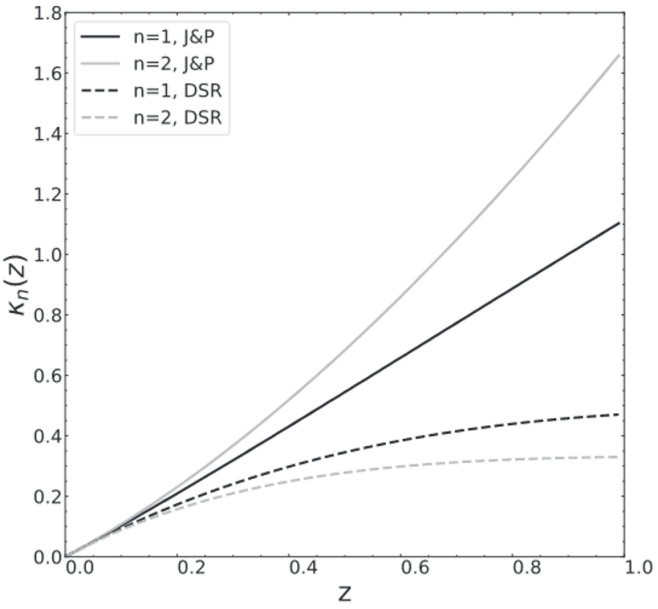

Figure 6: Comparison between J&P (solid line) and DSR (dashed line) lag-distance models through the κ_n parameter for both linear (black) and quadratic (gray) scenarios [32].

$$D\left(E_t, \lambda_n, z\right) = \lambda_n \times \kappa_n(z) \times E_t^n, \tag{20}$$

which characterizes the propagation lag due to LIV, where the redshift z is used as a free parameter. The normalization term N_s is described as follows:

$$N_s = \iint \Gamma_s\left(E_t\right) C_s\left(t - D\left(E_t, \lambda_n, z\right)\right) dE_t dt. \tag{21}$$

The C_s function present in Equations (19) and (21) is often called the template light curve and it is commonly obtained by fitting a light curve at low energies where LIV effects are considered to be negligible. To get the Γ_s function, the data on the entire energy range for the LIV analysis is taken into account.

Nevertheless, for a more realistic scenario, one must take into account the probability of detection of background events and add that term to the PDF. Background events are related mainly to two types: cosmic rays hadronic events that are gamma-like in footprint and are mis-reconstructed as signal events, and baseline events which are actually photons from the continuous emission of the source in analysis. The origin of the photons from the last category is different depending on the source in study: for pulsars, the baseline emission corresponds to the surrounding nebula, whose emission typically dominates the pulsar itself; for AGNs, the baseline refers to the source's quiescent state; and for GRBs, the baseline emission is generally negligible as its events are generated from an extremely powerful explosion that overshadows that surrounding continuous emission [2]. In either of these scenarios, the continuous emission can be described by a power-law energy distribution ($\Gamma_{b,k}$) with a given spectral index α_b and a uniform temporal distribution ($C_{b,k}$) that is insensitive to the LIV transformation for k that is written as

$$F_{b,k}\left(E_t, t\right) = \frac{\Gamma_{b,k}\left(E_t\right) C_{b,k}}{N_{b,k}}, \tag{22}$$

with the normalization term defined as

$$N_{b,k} = \iint \Gamma_{b,k}\left(E_t\right) C_{b,k} dE_t dt. \tag{23}$$

Moreover, for a more realistic analysis, IRFs are also included in the PDF construction which allows an accurate estimation of the instrument's performance. In this case, it should be generic enough to be suitable for every type of gamma-ray observatory.

Finally, the entire definition of the PDF is

$$\begin{aligned}\frac{dP}{dE_m dt} = w_s \frac{\int A_{\text{eff}}\left(E_t, \vec{\varepsilon}(t)\right) \text{Mig}\left(E_t, E_m, t\right) \times F_s\left(E_t, t; \lambda_n\right) dE_t}{N'_s} \\ + \sum_k w_{b,k} \frac{\int A_{\text{eff}}\left(E_t, \vec{\varepsilon}(t)\right) \text{Mig}\left(E_t, E_m, t\right) \times F_{b,k}\left(E_t\right) dE_t}{N'_{b,k}},\end{aligned} \tag{24}$$

with source and background terms weighted by w_s and $w_{b,k}$ respectively. E_t still denotes the true energy and E_m corresponds to the measured energy; N'_s and $N'_{b,k}$ refer to the normalisation parameters. The set of factors $\vec{\varepsilon}(t)$ on which the effective area depends, varies with observation conditions and with the methodology used for event reconstruction and identification; being the corresponding IRFs provided by the H.E.S.S., MAGIC, and VERITAS collaborations. It is important to highlight that we are working with time-dependent IRFs.

Looking at (Equation (24)), one can detect that the profile likelihood computation is very time-consuming due to the complexity of the functions and the number of events that need to be scanned; a 1D plus 3D integral has to be computed for each event! In order to avoid several weeks of computational run time, pre-computation and tabulation for each type of event and all IRF files are done. After that, an interpolation is computed for the minimization of the likelihood; reducing the computational time to hours [2].

By summing the log-likelihood of all the events for a given source S, the confidence levels (CLs) or the derivation of lower limits on λ_n (and $E_{QG,n}$) can be obtained:

$$L_S(\lambda_n) = -\sum_i \log\left(\frac{dP}{dE_m dt}(E_{m,i}, t_i); \lambda_n\right). \tag{25}$$

Then, the combined log-likelihood L_{comb} is merely given by the sum of the individual log-likelihood functions $L_S(\lambda_n)$ obtained for all the sources and/or observation nights:

$$L_{comb}(\lambda_n) = \sum_{allsources} L_S(\lambda_n). \tag{26}$$

Lastly, taking into account the statistical and systematic uncertainties is crucial as they propagate through the use of the profile likelihood. So, systematic error terms are added to each source in the log-likelihood which is written as follows:

$$L(\lambda_n, \vec{\theta}) = L_S(\lambda_n, \vec{\theta}) + L_{\text{template}}(\vec{\theta}_C) + L_\gamma(\theta_\gamma) + L_B(\vec{\theta}_B) + L_{ES}(\theta_{ES}) + L_z(\theta_z), \tag{27}$$

$\vec{\theta}$ being the vector with all the nuisance parameters, where $\vec{\theta}_C$ corresponds to the parameters of the light-curve analytic parameterization, θ_γ is the power-law index of the signal events spectrum of the specific source, $\vec{\theta}_B$ refers to the ratio of signal and of background event numbers to the total number of events, θ_{ES} denotes the energy scale and θ_z indicates the distance or redshift. Some of these parameters depend on the instrument used for the observation. These parameters can be generally considered as following a normal distribution, and can then be written as :

$$L_x(\vec{\theta}) = \sum_i \frac{(\theta_{x,i} - \bar{\theta}_{x,i})^2}{2\sigma^2_{\theta_{x,i}}}. \tag{28}$$

4.2.1 Simulations

Simulations are very important to check the code results in a controlled environment as well as evaluate systematical and/or statistical uncertainties. Template light curve validation is crucial due to the complexity of fitting light curves as already mentioned previously, a light curve simulation code is also included in LIVelihood, which is able to run simulations for light curves as well as phasograms in the case of pulsars.

The previous section specified step by step how to build a combined log likelihood for different sources and observatories. The parameters needed to run the corresponding simulations are the light curve shape (or phasogram shape), the power-law index of signal and background, IRFs of each observatory including the effective area and energy migration matrixes handling time-dependency, redshift corresponding to each source in the study, injected time lag per energy and lastly, the number of events per signal and background.

So, in that scenario, LIVelihood was tested on six different sources already published by the consortium collaborations involved in this LIV combined analysis. Among the types of sources, a GRB, three different types of AGNs, and two pulsar phasograms were checked; moreover, Crab pulsar was observed and combined by two different observatories. The simulation was done using the instrument IRFs for these particular observations provided by H.E.S.S., MAGIC, and VERITAS.

The light curve was simulated by the LIVelihood code using the parameters showed in Table 2.

Source	Energy Range (TeV)	Time Range	Spectral Index Γ_s, Γ_b	Light-curve Shape	Number of Events Likelihood , Template	Background Proportion Hadronic, Baseline
GRB 190114*C*	0.3 – 2	60 – 1200 s	5.43, –	curved power law	726, –	0.055, 0
PG 1553 + 113	0.4 – 0.8	0 – 8000 s	4.8, 4.8	double Gauss	72,82	0.29, 0.15
Mrk 501	0.25 – 11	0 – 1531 s	2.2, 2.2	single Gauss	1800, –	0.39, 0
PKS 2155-304	0.28 – 4	0 – 4000 s	3.46, 3.32	5 asymmetric Gauss	2965,561	0., 0.02
Crab (M)	0.4 – 7	0.36 – 0.45	2.81, 2.47	single Gauss + Baseline	14869, –	0., 0.961
Crab (V)	0.2 – 10	0.37 – 0.43	3.25, 2.47	single Gauss + Baseline	22764, –	0., 0.964
Vela	0.06 – 0.15	0.50 – 0.60	3.9, 1.75	asymmetric Lorentzian	330820, –	0., 0.998

Table 2: Simulation configurations for each source.

From Figure 7 to Figure 10, one can see the diverse types of variability that can be observed for different types of sources. The corresponding fitted light curves are also shown in the various figures. The light curve shape varies considerably from one source to another, ranging from a relatively simple Gaussian distribution as for Mkn 501 in Figure 8 to overlapping five asymmetric Gaussian distributions like Figure 9 for PKS 2155-304, or even a power-law with no distinct peak

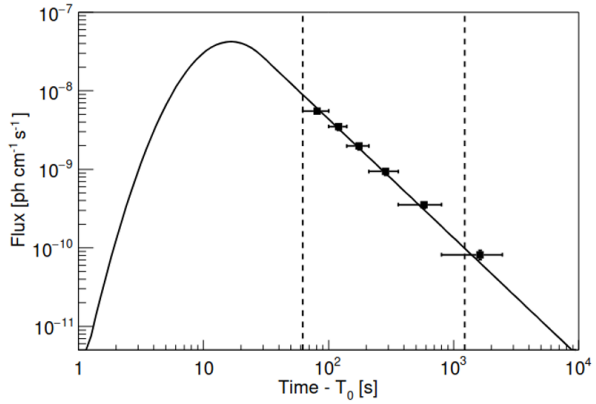

Figure 7: Intrinsic LC model of GRB 190114C; the points representing the γ-ray flux measured by MAGIC in the 0.3–1 TeV energy range [33].

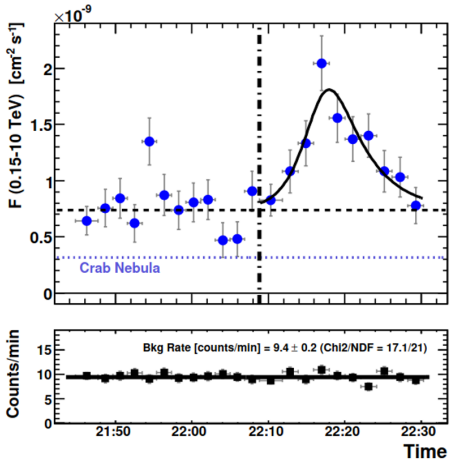

Figure 8: Integrated-flux LCs of Mrk 501 for the flare night of July 9 [34].

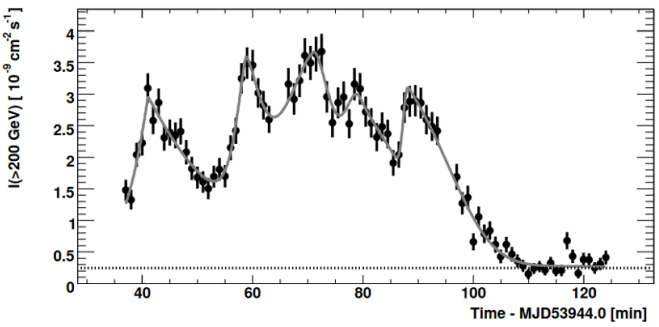

Figure 9: Integral flux above 200 GeV observed from PKS 2155-304 on MJD 53944 vs. time [35].

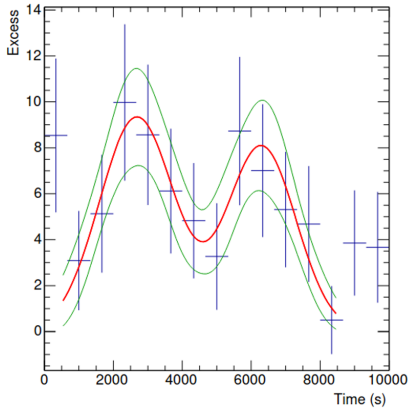

Figure 10: Time distribution of the excess for 6 runs with energies between 300 GeV and 400 GeV of PG 1553-133 [36].

as for GRB 190114C in Figure 7. Concretely for PG 1553-133, a combination of two Gaussian distributions is fitted (Figure 10).

Now, we must ensure that the method appropriately reconstructs the correction term λ_n for the analysis to produce reliable results. With that purpose, a thousand randomized simulated data sets for each source are created with a fixed and known value of λ_n being injected into each set. Those tests ensure the possibility of controlling the input and validating the method depending on the output.

As an example of the calibration tests executed on LIVelihood, Figure 11 shows the distribution of the reconstructed lag λ_n in the case of GRB 190114C for the linear case and using the J&P approach (central panel) with no injected lag. The distribution of reconstructed lag usually follows a Gaussian law but in the case of an asymmetric light curve, asymmetry is added to the final results distribution. The left and right panels show the distribution of the 1σ confidence intervals lower

limits $\lambda_{n,LL}$ and upper limits $\lambda_{n,UL}$ respectively, also fitted with an asymmetric Gaussian. Those limits were obtained using (Equation (25)) and determining the values of λ_n for which the likelihood function reduces to $2[L_S(\lambda_n - \min(L_S))] = 1$ for the 68% CL. It is important to highlight that the lower λ_{LL} and upper λ_{UL} limits take into consideration both statistical and systematic uncertainties. Also, that, all sources and data sets were fitted with asymmetric Gaussian functions in consistency.

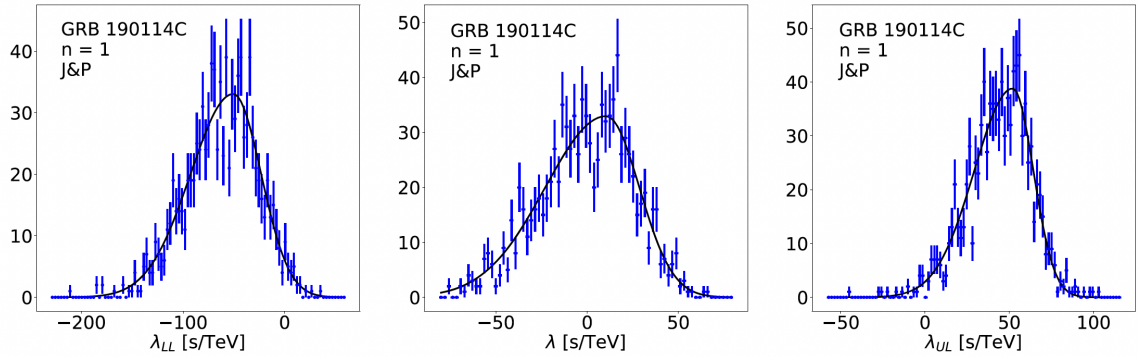

Figure 11: Distributions of the reconstructed lag (central panel), the corresponding lower limits (left panel), and upper limits for the 68% CL (right panel) for GRB 190114C. J&P formalism and linear scenario are applied with the injected lag being zero [32].

The plots of the reconstructed λ_{rec} and injected λ_{inj} lags were produced for each source as well as combinations of them to verify that the LIV analysis is well-behaved; linear and quadratic corrections and the two lag-distance models (J&P and DSR) were tested. Figure 12 displays two examples of calibration plots showing λ_{rec} versus λ_{inj} for GRB 190114C individually (left panel) and for the combination of all sources (right panel) in the linear and J&P case.

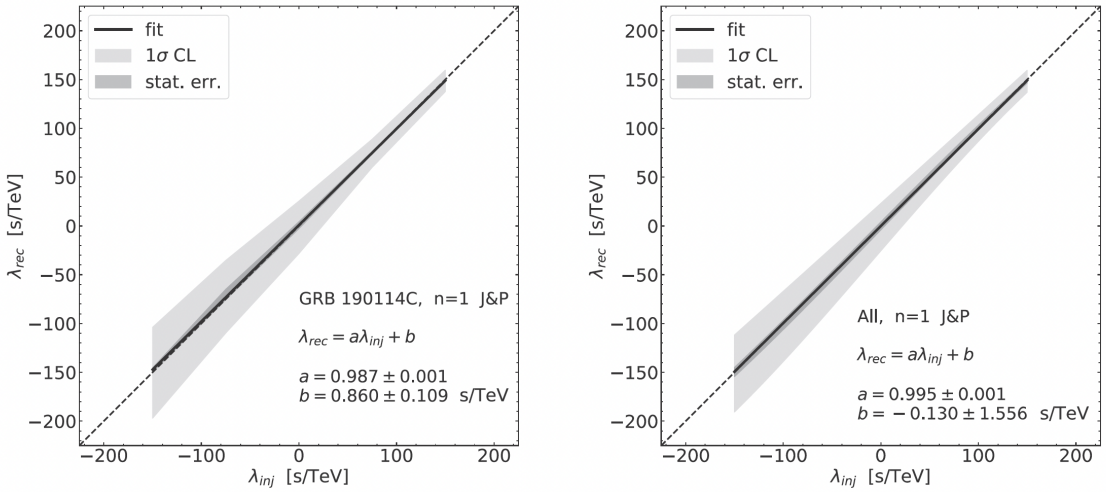

Figure 12: Calibration plots for the individual source GRB 190114C (left panel) and the combination of all sources (right panel) [32].

Finally, after the calibration tests, one can extract limits on $E_{QG,n}$ for each of the simulated sources and scenarios, meaning linear and quadratic behaviors and J&P and DSR redshift dependence. Figure 13 displays the lower limits obtained for the different sources and the combination of

all of them, in the linear case and for both DSR and J&P models; taking into account only statistical errors and also when both systematic and statistical errors are included.

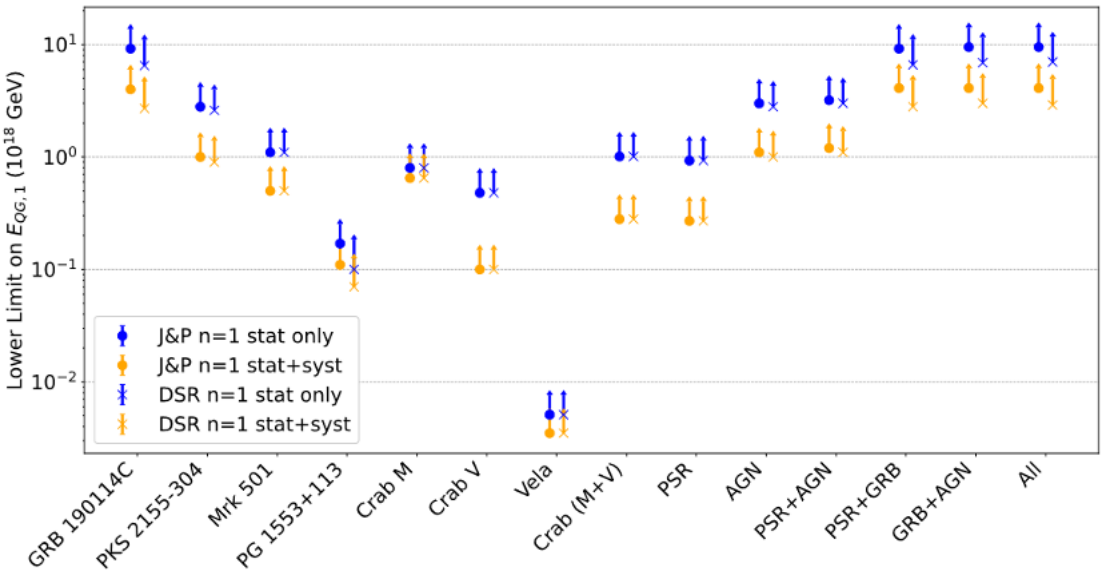

Figure 13: Comparison between the limits on $E_{QG,n}$ with and without systematic uncertainties for the two lag-distance models and linear correction order [32].

To sum up, let us see how these limits behave with redshift. Figure 14 shows the limits of $E_{QG,n}$ as a function of redshift for both J&P and DSR methods. Differences between the two approaches begin to take relevance for high-redshift sources, in concordance with what we discerned in Figure 6. Besides, there are three effects that rule over the redshift variability of the limit: the distance as just mentioned, the EBL absorption where mostly the high energy events are absorbed, and the fact that the delay increases with redshift.

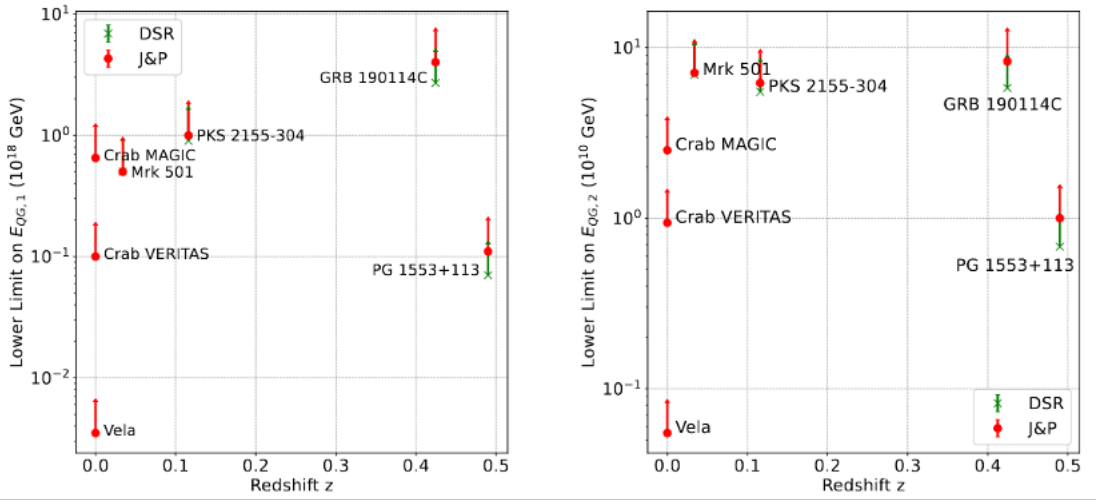

Figure 14: Comparison between the limits on $E_{QG,n}$ for J&P and DSR models for the two correction orders [32].

4.3 LIVelihood tutorial

The aim of the tutorial section is to perform LIV data analysis on a simulated signal. This is a summary of the steps performed in the school by the students.

4.3.1 Source analysis

The first step is to get the data needed for the simulation of the source that we want to analyze: in our case, the data used came from a flaring AGN, PKS 2155-304 observed by H.E.S.S. during the night from July 29 to 30 2006 [37]. For this, Gammapy, an open-source Python package for gamma-ray astronomy [38], is used. In summary, we have to:

- Select relevant `gammapy.data.Observations` from the `gammapy.data.DataStore`,
- Apply the time selection in our predefined time intervals to obtain a new, `gammapy.data.Observations`
- Perform the data reduction (in 1D or 3D),
- Define the source model,
- Extract the light curve from the reduced dataset.

Frequently, especially when studying flares of bright sources, it is necessary to explore the time behavior of a source on short time scales, in particular on time scales shorter than observing runs.

Once we have the data, Gammapy produces datasets in a given time interval, by default that of the parent observation. To be able to produce datasets on smaller time steps it is necessary to split the observations into the required time intervals. This is easily performed with the `select_time` method of `gammapy.data.Observations`.

After the data is uploaded and the observations selected, we create the list of time intervals. Each time interval is an `astropy.time.Time` object, containing a start and stop time. We then apply the list of time intervals to the observations with the `select_time` method. This returns a new list of `gammapy.data.Observations` objects filtered by `time_intervals`. For each time interval, a new observation, of duration equal to the chosen time step, is created that converts the intersection of the good time intervals, defined as the time intervals that can be safely used in the run, and time interval.

We can then proceed with data reduction and for the sake of the tutorial we are going to perform the data reduction in 1D with reflected regions, building 1D datasets from the new observations. Beware that with small time intervals, the background normalization with OFF regions might become problematic. In order to build the datasets we must first define a geometry, specifying the energy axes and defining the ON extraction region. As usual, the true energy axis has to cover a wider range to ensure good coverage of the measured energy range chosen. The size of the ON extraction region follows typical spectral extraction regions for H.E.S.S. analyses. Once the geometry is set we can proceed with the creation of the data reduction makers and finally create the 1D datasets, i.e. perform the actual data reduction in the `time_intervals`.

Finally, we can define a model for the signal and then proceed with the extraction of the lightcurve from the reduced datasets in order to get all the source characteristics necessary for

the next step of the LIV analysis. Beware that the actual flux will depend on the spectral shape assumed, but for simplicity, in the tutorial, we used the power law spectral model of index 3.4 used in the reference paper [37]. The power law spectral model can be found in the `gammapy.modeling.models.SkyModel` object.

For the extraction of the lightcurve, we first need to create the gammapy *LightCurveEstimator* for the list of datasets we just produced and then perform the light curve extraction itself. To compare with the reference paper [37], we select the 0.7-20 TeV range. Finally, we fit the lightcurve with a Gaussian model and extract the source characteristics required for the next step of the LIV analysis. The complete list of parameters can be found in the next exercise.

4.3.2 Source simulation and analysis with LIVelihood (without IRFs)

LIVelihood can use the parameters extracted in the first exercise in order to perform simulations of the source.

We proceed to simulate the source based on the analysis made and then perform a LIV analysis supposing that the reconstruction of the instrument is perfect (no energy migration, flat effective area versus energy). The parameters obtained in the previous exercise and needed to perform simulations are :

- Energy range,
- Time range,
- Light curve parameters (the parameters of the Gaussian fitted in the previous exercise)
  - mean
  - fit limits
  - width
  - normalization
  - delay,
- The power law distribution of the events
  - spectral index
  - parameter limits
  - normalization,
- Proportion of signal and background
  - percentage of signal
  - percentage of hadronic background
  - power law spectral index for hadronic bkg
  - power law spectral index for baseline signal,
- Redshift of the source.

From these parameters, simple Monte-Carlo simulations are performed. LIV analysis is performed from these simulations. These simulations inject a delay of 0 s/TeV so you should reconstruct zero in the mean. The resulting distribution of the delay per energy is plotted in Figure 15, as well as the 95% confidence interval. It is possible to inject a fake LIV effect in the simulations in order to check that it is well reconstructed. This kind of check is mandatory to be sure that the software is able to

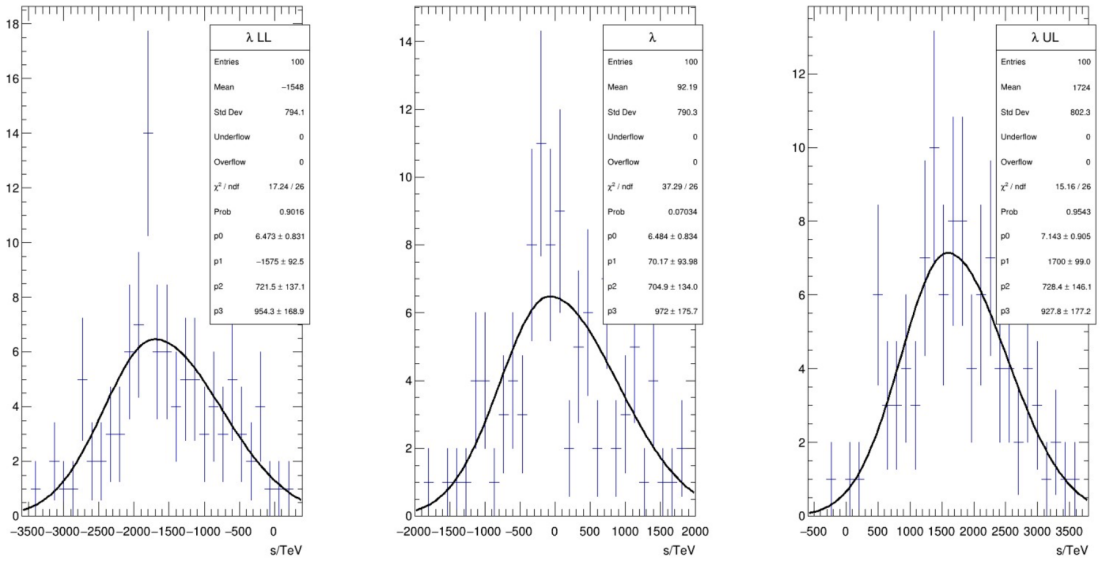

Figure 15: Fit results from simulation of a signal with a delay of 0 s/TeV

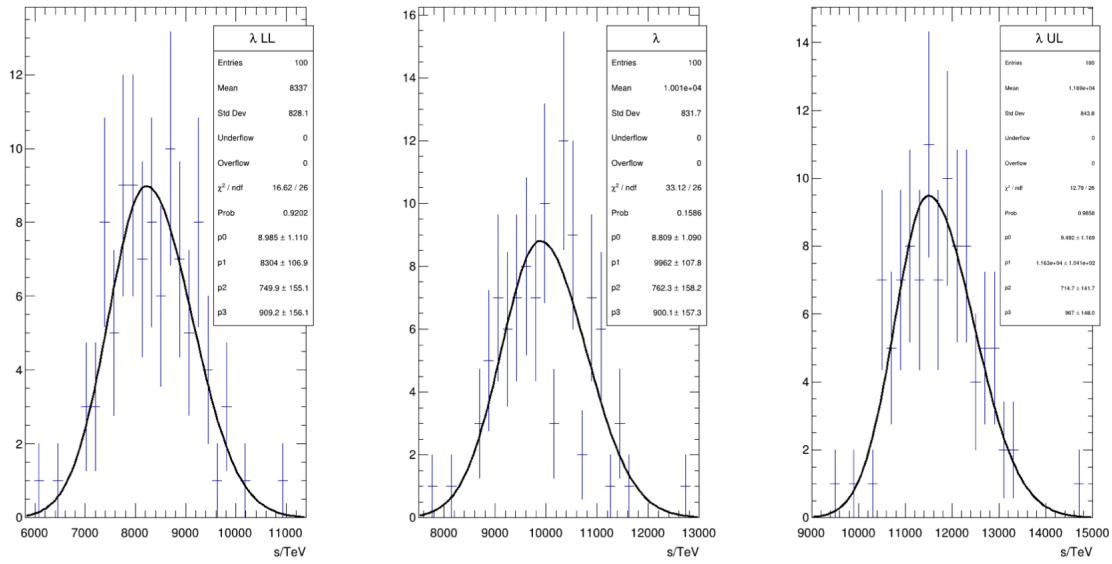

Figure 16: Fit results from Simulation of a signal with a delay of 10000 s/TeV

reconstruct properly the LIV effect. To do so we repeat the prompts used earlier, this time adding the time delay. The result can be seen in Figure 16 with an injected delay of 10000 s/TeV. Mean reconstructed lag is indeed 10000 s/TeV matching the value we injected in the simulations: we got here a clear detection, incompatible with 0 s/TeV. Injecting smaller time delays (e.g. 2000 s/TeV) would yield analog results, with the correct mean reconstructed lag, but with lower significance. The statistical uncertainty of this measurement is approximately 2000 s.TeV^{-1} which is 5 times less than the reconstructed lag, so a 5 σ detection.

Beware that up to this point we just simulated signals supposing a perfect instrument, without

taking into account any systematics.

4.3.3 A bit of uncertainty

It is very important to take into account the systematical uncertainty of the apparatus used for the observations. These are all the assumptions made in the previous exercise:

- the energy is always perfectly reconstructed for all events,
- the amount of background is perfectly known,
- there is no uncertainty on the temporal distribution of the events,
- no uncertainty on the spectral distribution of events,
- no uncertainty on the redshift.

The systematics of the H.E.S.S. observatory are already contained in the LIVelihood code and can be taken into account through the `test_runner` command. Let's repeat the prompts used in the previous exercise and add now the systematics. This time, as expected, the reconstructed distribution of the parameters is wider and the quantum gravity limit is less constraining. In this example, we now have a mean lambda of approximately 10000 ± 4500 so we only have a $\sim 3\sigma$ significance when accounting for systematics, as opposed to the 5 σ detection we had previously if we take into account systematics (see Figure 17).

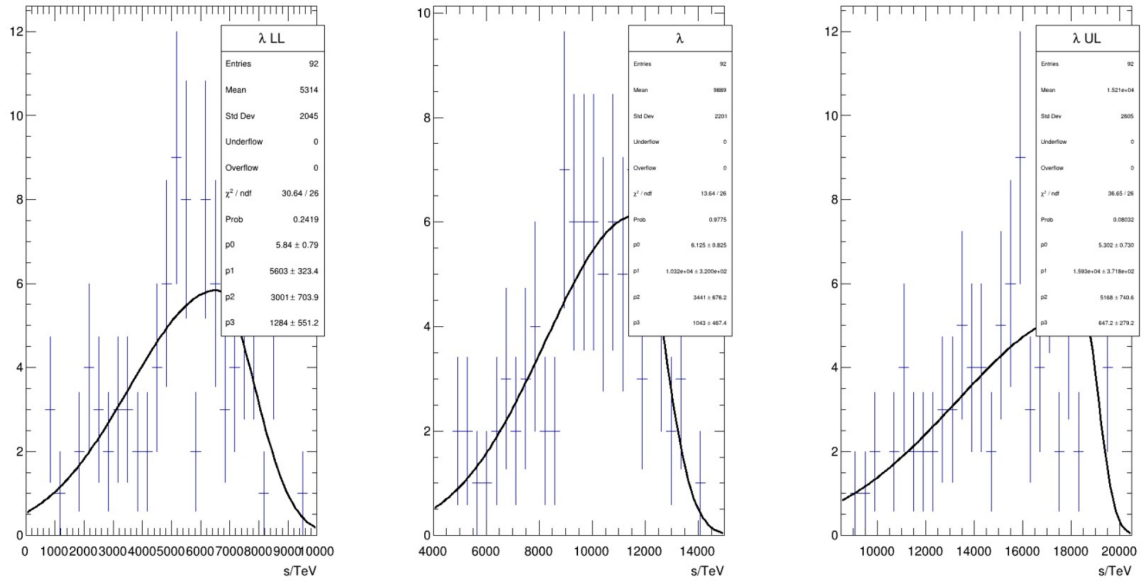

Figure 17: Results from simulations of a signal with a delay of 10000 s/TeV, including the systematic uncertainties.

4.3.4 Interlude, from the DL3 data to the ON OFF DL3

DL3 data contain all the gamma-like events in the field of view. For the LIV analysis, we are interested in the amount of events in the direction of the source, within a certain angular region that we used for the high-level analysis. In this step, we need as well to extract the energy distribution of the background. Indeed we are not interested in all the events in the field of view but only in events in the so-called region of interest around the source, and the associated background sampled.

4.3.5 Analysis and simulation with the IRFs (effective area only)

LIVelihood can use the IRFs contained in the DL3 files to perform a more realistic simulation. The likelihood, in this case, is precomputed in tables, to not perform the same computation for each event added to the global likelihood.

The results, with only the effect of the effective area, can be seen in Figure 18. Monte Carlo

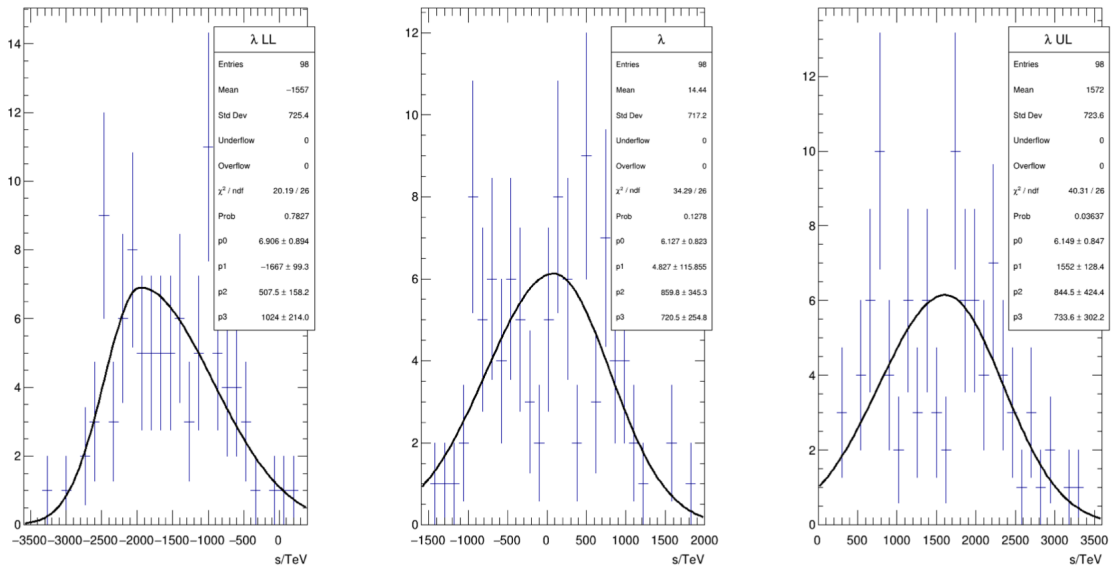

Figure 18: Results from simulations with a delay of 0 s/TeV, including the systematic errors and simulating the effect of the effective area versus the energy.

simulations can be directly accessed. For example, the plots of the effective area versus the log of energy for all the events as shown in Figure 19. It is possible to see that different runs have different effective areas (this is mostly due to the variability of the zenith angle during the night). Finally,

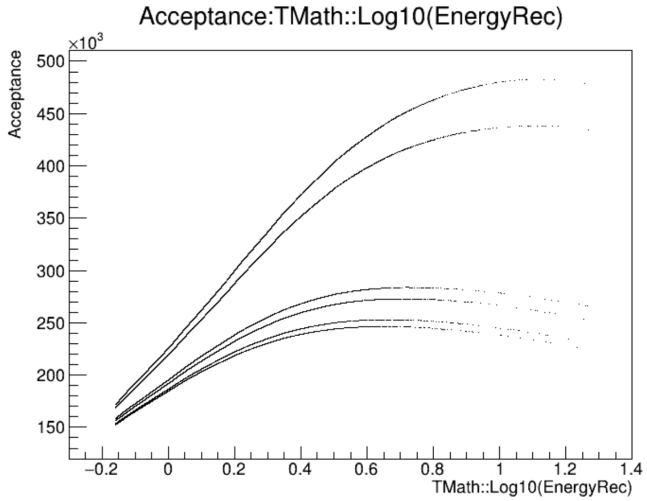

Figure 19: Acceptance versus the log of energy.

performing again the simulations, injecting a 10000 s/TeV time lag but this time taking into account the effective area, we obtain the results in Figure 20. As you can see, the lag is well reconstructed (Mean Lambda: $(1.002 \pm 0.08394) \times 10^4$ s/TeV).

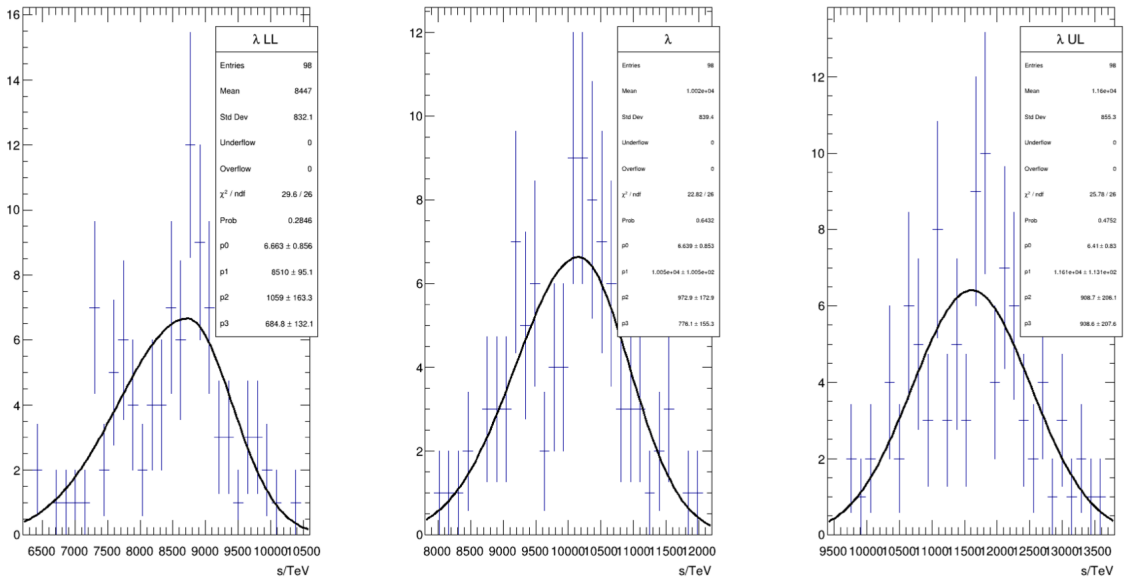

Figure 20: Simulation of a signal with a delay of 10000 s/TeV, including the systematic errors and simulating the effect of the effective area versus the energy.

4.3.6 Analysis with IRFs (energy migration)

This time we will take into account the energy migration as well. In simulations, it implies another step that consists of generating reconstructed energy thanks to the migration matrix. The results can be seen in Figure 21.

A bias can be observed, this is generally due to the precision of the tables. As it takes a lot of time to improve the precision of the table, it is beyond the scope of these notes to focus on that. Since the bias is less important than the statistical uncertainty, the result/outcome is barely modified. Let's have a look at the Monte Carlo simulations again, this time focusing on the detector response matrix. You can find the result in Figure 22. It is interesting to see that the binning is visible in the data. Another way of improving this measurement can be to increase the matrix binning (see Section 4.3.4), this is particularly important since the events are distributed as a power law, and so the low energy dominates the distribution.

4.3.7 Different types of simulations; simulations based on real data

LIVelihood can handle 3 different types of simulations:

- Full simulations (the standard way, used in all the tutorials before)
  - Events are simulated from the spectra and light curve and the IRFs,
  - caveat: we have to suppose a spectrum for the background (2.7) and suppose that they follow the same IRFs as gamma-like,

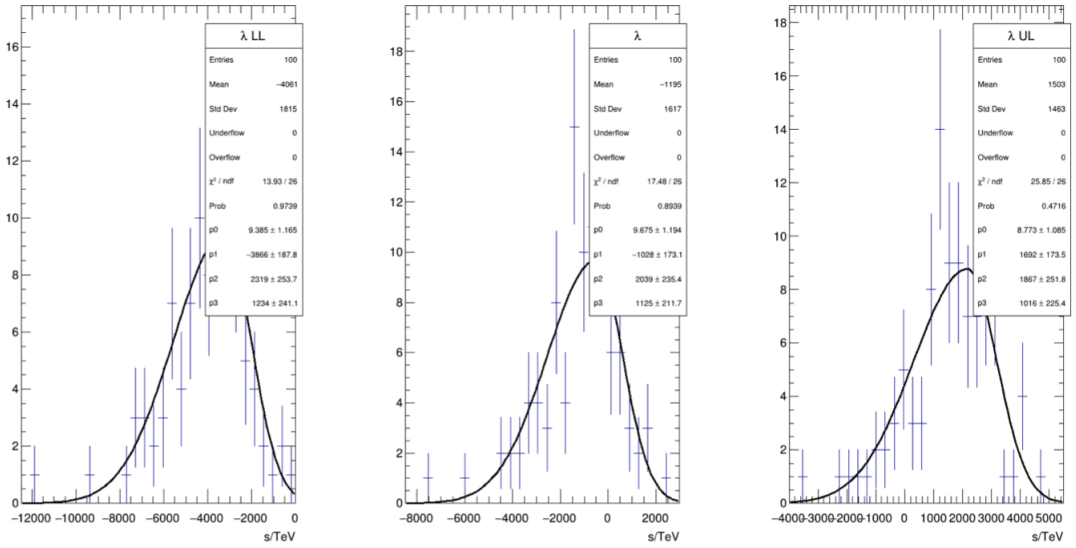

Figure 21: Simulation of a signal with a delay of 10000 s/TeV, including the systematic errors, simulating the effect of the effective area versus the energy and considering also the energy migration.

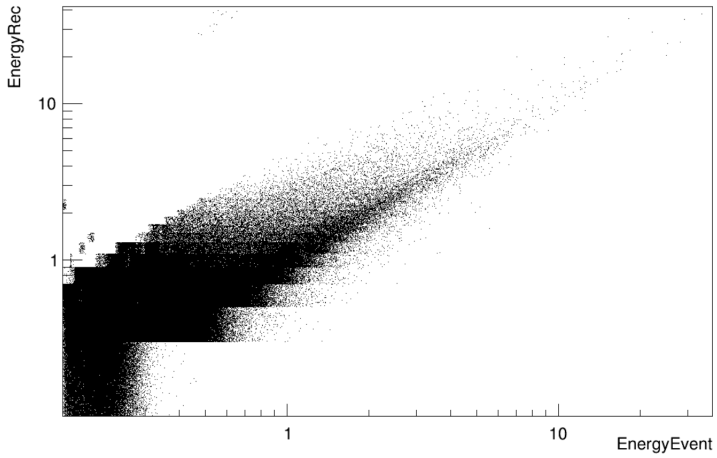

Figure 22: Response matrix for a simulation of a signal with a delay of 10000 s/TeV, including the systematic errors, simulating the effect of the effective area versus the energy and considering also the energy migration.

- OFF simulations:
  - the signal is simulated thanks to full simulation,
  - the background is simulated from the distribution of OFF event in the DL3,
  - Should be more realistic but depends on the OFF event stat in the DL3,
  - It is completely useless for sources where the background is negligible (this one for example),
- ON OFF simulations:
  - the signal and background are simulated from ON and OFF regions,

– Permits to re-simulate real data, the results obtained from this simulation can be considered as real results, and their spread as the uncertainty of the analysis.

Let's try with the third one.

This time the limit will use real data. The results can be seen in Figure 23 and show a positive $\sim 2\sigma$ lag, compatible with a statistical fluctuation.

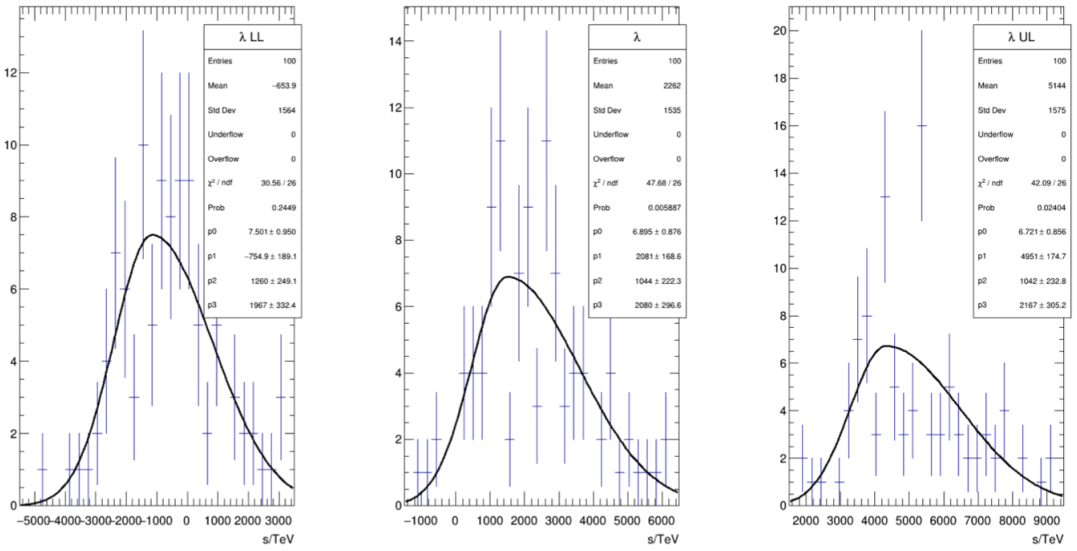

Figure 23: Distribution of results from the toy Monte-Carlo simulations obtained from the real data.

5. Future

In this course, the state-of-the-art LIV analysis , based on energy-dependent time lag, was presented. But several improvements can be seen in the future.

In general, the light curve parameterization is a process that is not completely defined. The choice of the binning and of the function used to perform the fit is partial. It is particularly difficult to assess the optimal binning for such models. Several methods should be developed in the future to permit a smoother derivation of this, as well as the development of optimized binning to catch fast variability. The sensitivity jump of CTA will need such improvements because faster variability will be possible to be detected. Light curve parameterization could be used as well physically motivated models which can make the choice of the light curve model less partial.

Another important point for future studies is probably the detection of energy distribution variability of the source flux for a timescale of the order of the night. All the current techniques are based on time-independent spectra, which is justified today because of the lack of statistics of the current experiments. The likelihood can easily use a time and energy-dependent probability density function, allowing to exploration of data with time-dependent energy distribution, but this can likely generate some LIV-like effect and degeneracy in the fit. Physically motivated modeling can help to disentangle this from the LIV effect, but the solution will likely come from a joint analysis of sources. No redshift dependence is expected for such an effect in first approximation,

while stochasticity for different flares and sources is expected. The combination of multiple sources will not only be needed to improve the results but as well to understand the likely stochastic time-lag that will be observed in case of detectable source intrinsic effect.

Finally the problem of the distinction between LIV time lag and astrophysical time lag is still not an issue today, since no time lag at all is detected. Possible detection of time lag due to a jump in sensitivity will probably require future analysis, and analyzers, to deal with this issue.

Acknowlegments

ACO is gratefully acknowledged by the financial support of the Spanish grant PID2019-107847RB-C42, funded by MCIN/AEI/ 10.13039/501100011033. Finally, the authors would like to acknowledge networking support by the COST Action CA18108. We gratefully acknowledge financial support from the Labex ENIGMASS.

References

[1] U. Jacob and T. Piran, *Lorentz-violation-induced arrival delays of cosmological particles*, *Journal of Cosmology and Astroparticle Physics* **2008** (2008) 031.

[2] C. Levy, *Energy dependent time delays induced by Lorentz Invariance Violation: discriminating source-intrinsic effects with blazar modeling and preparation of population studies with H.E.S.S. MAGIC and VERITAS.*, theses, Sorbonne Université, Nov., 2021.

[3] and H. Abdalla, F. Aharonian, F.A. Benkhali, E.O. Angüner, M. Arakawa, C. Arcaro et al., *Particle transport within the pulsar wind nebula HESS j1825–137*, *Astronomy &amp Astrophysics* **621** (2019) A116.

[4] J. Aleksić, S. Ansoldi, L. Antonelli, P. Antoranz, A. Babic, P. Bangale et al., *Measurement of the crab nebula spectrum over three decades in energy with the MAGIC telescopes*, *Journal of High Energy Astrophysics* **5-6** (2015) 30.

[5] C. Kouveliotou, C.A. Meegan, G.J. Fishman, N.P. Bhat, M.S. Briggs, T.M. Koshut et al., *Identification of Two Classes of Gamma-Ray Bursts*, ApJ **413** (1993) L101.

[6] M.T. et al, *Particle Data Group: Chapter 29 - Cosmic Rays*, Phys. Rev. D (2019).

[7] "CTA observatory." https://www.cta-observatory.org/about/how-cta-works/.

[8] R.M. Wagner, *Measurement of very high energy gamma-ray emission from four blazars using the MAGIC telescope and a comparative blazar study*, Ph.D. thesis, Max-Planck-Institute for Physics, Munich, Jan., 2006.

[9] "H.E.S.S. collaboration." https://www.mpi-hd.mpg.de/HESS/pages/about/telescopes/.

[10] T. Garrigoux, *Étude des emissions diffuses avec l'expérience H.E.S.S.*, theses, Université Pierre et Marie Curie - Paris VI, May, 2015.

[11] F. Aharonian, A.G. Akhperjanian, A.R. Bazer-Bachi, M. Beilicke, W. Benbow, D. Berge et al., *Observations of the Crab Nebula with H.E.S.S.*, *Astronomy & Astrophysics* **457** (2006) 899.

[12] G. Giavitto, S. Bonnefoy, T. Ashton, M. Backes, A. Balzer, D. Berge et al., *Performance of the upgraded H.E.S.S. cameras*, in *35th International Cosmic Ray Conference (ICRC2017)*, vol. 301 of *International Cosmic Ray Conference*, p. 805, July, 2017, DOI [1708.04550].

[13] J. Cortina, F. Goebel and T. Schweizer, *Technical Performance of the MAGIC Telescopes*, 2009.

[14] J. Aleksić, E. Alvarez, L. Antonelli, P. Antoranz, M. Asensio, M. Backes et al., *Performance of the magic stereo system obtained with crab nebula data*, *Astroparticle Physics* **35** (2012) 435.

[15] S.M. Bradbury, I.H. Bond, A.C. Breslin, J.H. Buckley, D.A. Carter-Lewis, M. Catanese et al., *The Very Energetic Radiation Imaging Telescope Array System (VERITAS)*, 1999.

[16] J.-F. Rajotte, *Upgrade and performance of the veritas telescope array*, *Nuclear Instruments and Methods in Physics Research Section A: Accelerators, Spectrometers, Detectors and Associated Equipment* **766** (2014) 61.

[17] H. Abe, K. Abe, S. Abe, A. Aguasca-Cabot, I. Agudo, N. Alvarez Crespo et al., *Observations of the Crab Nebula and Pulsar with the Large-sized Telescope Prototype of the Cherenkov Telescope Array*, ApJ **956** (2023) 80 [2306.12960].

[18] O. Gueta, *The Cherenkov Telescope Array: layout, design and performance*, in *Proceedings of 37th International Cosmic Ray Conference — PoS(ICRC2021)*, Sissa Medialab, jul, 2021, DOI.

[19] D. Mazin, H. Abe, A. Aguasca, I. Agudo, L.A. Antonelli, C. Aramo et al., *Status and results of the prototype LST of CTA*, in *Proceedings of 37th International Cosmic Ray Conference — PoS(ICRC2021)*, Sissa Medialab, jul, 2021, DOI.

[20] J. Bolmont et al., *Gamma-ray data collection, calibration and analysis*, in *Proceedings of the COST CA18108 Second Training School — PoS(QG-MMSchools)003*, Sep, 2022.

[21] D. Berge, S. Funk and J. Hinton, *Background modelling in very-high-energy gamma-ray astronomy*, *Astronomy & Astrophysics* **466** (2007) 1219.

[22] M. Martínez and M. Errando, *A new approach to study energy-dependent arrival delays on photons from astrophysical sources*, *Astroparticle Physics* **31** (2009) 226.

[23] T.-P. Li and Y.-Q. Ma, *Analysis methods for results in gamma-ray astronomy.*, ApJ **272** (1983) 317.

[24] J. Holder, R.W. Atkins, H.M. Badran, G. Blaylock, S.M. Bradbury, J.H. Buckley et al., *The first VERITAS telescope*, *Astroparticle Physics* **25** (2006) 391 [astro-ph/0604119].

[25] J. Aleksić, E. Alvarez, L. Antonelli, P. Antoranz, M. Asensio, M. Backes et al., *Performance of the MAGIC stereo system obtained with crab nebula data*, *Astroparticle Physics* **35** (2012) 435.

[26] J.A. Hinton and HESS Collaboration, *The status of the HESS project*, New A Rev. **48** (2004) 331 [astro-ph/0403052].

[27] "Lst technology." https://www.cta-observatory.org/project/technology/lst/.

[28] "Mst technology." https://www.cta-observatory.org/project/technology/mst/.

[29] "Sst technology." https://www.cta-observatory.org/project/technology/sst/.

[30] J.D. Finke, M. Ajello, A. Domínguez, A. Desai, D.H. Hartmann, V.S. Paliya et al., *Modeling the Extragalactic Background Light and the Cosmic Star Formation History*, ApJ **941** (2022) 33 [2210.01157].

[31] F. Aharonian, J. Aschersleben, M. Backes, V.B. Martins, R. Batzofin, Y. Becherini et al., *Constraints on the intergalactic magnetic field using fermi-lat and h.e.s.s. blazar observations*, *The Astrophysical Journal Letters* **950** (2023) L16.

[32] J. Bolmont, S. Caroff, M. Gaug, A. Gent, A. Jacholkowska, D. Kerszberg et al., *First Combined Study on Lorentz Invariance Violation from Observations of Energy-dependent Time Delays from Multiple-type Gamma-Ray Sources. I. Motivation, Method Description, and Validation through Simulations of H.E.S.S., MAGIC, and VERITAS Data Sets*, *The Astrophysical Journal* **930** (2022) 75.

[33] V. Acciari, S. Ansoldi, L. Antonelli, A.A. Engels, D. Baack, A. Babić et al., *Bounds on Lorentz Invariance Violation from MAGIC Observation of GRB 190114C*, *Physical Review Letters* **125** (2020) .

[34] J. Albert, E. Aliu, H. Anderhub, P. Antoranz, A. Armada, C. Baixeras et al., *Variable very high energy γ-ray emission from markarian 501*, *The Astrophysical Journal* **669** (2007) 862.

[35] F. Aharonian, A.G. Akhperjanian, A.R. Bazer-Bachi, B. Behera, M. Beilicke, W. Benbow et al., *An exceptional very high energy gamma-ray flare of pks 2155–304*, *The Astrophysical Journal* **664** (2007) L71.

[36] A. Abramowski, F. Aharonian, F.A. Benkhali, A.G. Akhperjanian, E.O. Angüner, M. Backes et al., *The 2012 flare of PG 1553+113 seen with H.E.S.S. and Fermi-LAT*, *The Astrophysical Journal* **802** (2015) 65.

[37] F. Aharonian et al., *Simultaneous multiwavelength observations of the second exceptional γ-ray flare of PKS 2155-304 in July 2006*, A&A **502** (2009) 749 [0906.2002].

[38] C. Deil et al., *Gammapy - A prototype for the CTA science tools*, in *35th International Cosmic Ray Conference (ICRC2017)*, vol. 301 of *International Cosmic Ray Conference*, p. 766, Jan., 2017 [1709.01751].